Quantifying degradation mechanisms in a high performance parallel hybrid lithium-ion supercapacitor induced by long term cycling at high current rates

Victor Vanpeene, I. Martens, M. Mirolo, A. Benayad, L. Daniel, S. Geniès, Y. Maletin, N. Stryzhakova, S. Zelinskyi, S. Chernukhin, et al.

Quantifying degradation mechanisms in a high performance parallel hybrid lithium-ion supercapacitor induced by long term cycling at high current rates

V. Vanpeene[a,*], I. Martens[a], M. Mirolo[a], A. Benayad[b], L. Daniel[b], S. Geniès[b], Y. Maletin[c], N. Stryzhakova[c], S. Zelinskyi[c], S. Chernukhin[c], J. Drnec[a], J. Villanova[a,*]

[a] *ESRF-The European Synchrotron, F-38000 Grenoble, France.*

[b] *Université Grenoble Alpes, CEA-LITEN, 17 rue des Martyrs, 38054 Grenoble Cedex 9, France.*

[c] *Yunasko-Ukraine LLC, 03164 Kyiv, Ukraine.*

* Corresponding authors:

E–mail: victor.vanpeene@esrf.fr (V. Vanpeene); julie.villanova@esrf.fr (J. Villanova)

Abstract

Understanding the degradation pathways of electrode materials is a key to develop more reliable Li-ion technologies along with an increased energy density and power rate. This study aims to demonstrate the benefits of the combined use of X-ray based characterization techniques and electrochemical assessment for thorough multi-scale anlaysis to elucidate the aging mechanisms of a $Li_4Ti_5O_{12}$/AC//$LiMn_2O_4$/AC parallel hybrid lithium-ion supercapacitor. Analyses performed on samples extracted from full stack representative of industrial battery application, show that irreversible modifications are observed at all length scales on both electrodes. At the negative, the disaggregation and corrosion of the LTO active material, as well as AC particle cracking and electrode film delamination have been observed. In the meantime, drastic cracking of the AC and LMO active material along with important micro-strain increase at the crystallite level for LMO as well as Mn^{3+} dissolution are reported at the positive. The formation of a cathode electrolyte interface (CEI) is also reported. These structural and chemical changes have been identified as precursors to important polarization increase, Li inventory loss and furthermore capacity fading leading thus to device failure.

Keywords: Li-ion supercapacitor; hybrid parallel; LTO; LMO; X-ray nano-tomography; X-ray diffraction; X-ray photoelectron spectroscopy

1. Introduction

During the past decades, a variety of lithium-ion battery chemistries have been investigated to tackle the challenges arising from the large-scale deployment of electric vehicles, including higher energy and power density, fast charge capabilities, cycle stability, lower costs, and safer operation **[1,2]**. In this context, lithium-ion capacitors (LICs) have raised significant interest over the past decades as energy storage device with high power density, which combines the advantages of a lithium-ion battery (LIB) and an electric double-layer capacitor (EDLC) **[3-7]**. The principles of internal hybridization of electrochemical systems of supercapacitors (SC) and batteries at the level of electrode materials and electrolytes are now well established **[8,9]**. The first hybrid systems displaying asymmetric or so called "serial" connection of electrodes using SC alternated with battery technology were invented in the late 90's **[10]** and included nano-porous carbon at the negative electrode and nickel hydroxide at the positive electrode. The hybrid system doubled the energy density of standard SCs commonly constituted of carbon/carbon symmetric electrodes, from 20-30 to 40-50 kJ/kg. Later, a serial hybridization with mixt SC/LIB components along the same electrode has also been successfully performed, designated consequently as LIC (Li-ion capacitor) **[3,5,8]**. As for battery technology, LICs commonly use graphite-based materials, although mostly turbostratically disordered carbon ("hard carbon") **[11],** or more rarely lithium titanate, $Li_4Ti_5O_{12}$ **[3]** at the negative electrode. JSR Micro Co pioneered the industrial development of LIC **[12,13]**, with hybrid capacitors and prismatic modules with operating voltages of 15.2 V for a capacity of up to 800 F (ULTIMO, 168×127×112 mm^3), showing excellent discharge currents and long cycle life. Asymmetric or serial hybridization can only increase the capacity of common SCs by a factor two since their total capacity is still limited by the capacity resulting from the electric double layer. Hence, ULTIMO modules have limited specific energy in the range of 40-50 kJ/kg **[13]**. Nevertheless, an effective way to

overcome this limitation lies in the increase of both positive and negative electrodes capacities, by mixing LIB and SC components at both the negative and positive electrode. The theoretical justification of such a symmetric solution, so called "parallel" hybrid, has been thoroughly detailed in the study of D. Cericola and R. Kotz **[8]**. The same concept has been implemented and further described in our works **[11,14]**.

Since the first reports of Amatucci *et al.* in 2001 presenting an asymmetric hybrid battery supercapacitor constituted of a lithium titanate negative electrode paired to an activated carbon (AC) positive electrode **[3]**, numerous alternatives have been investigated [**6,8,15**]. The main requirements for achieving high cycle performance encompass a stable active material structure along with mitigated degradation of the electrolyte during the device operation. Thus, $Li_4Ti_5O_{12}$ (LTO) negative and $LiMn_2O_4$ (LMO) positive materials applied in hybrid battery capacitors have already received particular interest **[3,6,7,16]**. Their spinel structures require very low lattice distortion for lithium ion intercalation/deintercalation, yielding high reversibility, while also containing efficient 3D ion conduction channels. These characteristics **[17]** make spinels interesting candidates as active materials in high power devices with long cycle-life **[18-20]**. In addition, the relatively high voltage of LMO positives leads to an increase in the energy density of the cell **[21]**, suitable towards next generation high energy density application **[22]**. In fact, the comparative study of different hybrid systems based on LTO, LMO and AC performed by D. Cericola *et al.* **[6]** suggest that such hybrid systems would help achieving high power/energy devices with outmost benefits in pulsed applications. However, only few reports in the literature are focused on the pairing of composite hybrid LMO/AC and LTO/AC electrodes together **[6,23]** and the related degradation mechanisms are still poorly understood.

Despite these advantages in reaction kinetics and higher operating voltage, the adoption of LTO at the negative electrode in LIB systems is still limited by their tendency towards gas

generation during cycling and calendar aging, especially above ambient temperatures **[24,25**], even when combined with AC for high rate application **[26]**. Electrolyte degradation at the LTO surface generates H_2, CO_2 and CO, leading to swelling of the device. On top of the safety concerns, gas generation also triggers rapid aging of the cell. This has been attributed to the loss of active material connectivity and partial electrode delamination resulting from pressure gradients and bubble evolution **[27,28]**. This gas swelling issue has been thoroughly studied in the literature for lithium-ion batteries (LIBs) but few reports are available on LICs systems, where high C-rate and different electrolyte composition might affect this behavior. On the positive electrode side, LMO shows a tendency towards Mn dissolution, crossover, and poisoning of the negative electrode. In fact, Mn ions have been observed on the negative electrode of aged LMO|LTO LIB cells by ToF-SIMS **[29]**, NEXAFS/HAXPES **[30]**, and other techniques **[24]**. These diverse failure modes are typical for battery materials, but the extent to which each of these potential degradation processes contribute towards actual performance loss inside hybrid parallel LICs functional devices is not clear, and not well studied in the literature. Moreover, it depends on a cell's form factor, electrode fabrication, cycling history, and other commercially important considerations in a large cell assembly configuration. Unfortunately, the cell geometry and analytical workflows for many studies (*e.g.*, in situ TEM) are incompatible with full devices, and cannot replicate the multiple processes, which cooperatively produce cell failure. In this work, we show how a combined set of characterization techniques provide a holistic perspective of the aging mechanisms inside a full-size, commercial LMO/AC|LTO/AC hybrid LIC, subjected to a realistic (accelerated) combined cycling-calendar aging life cycle, using samples extracted from the full pack. Understanding and validating the relevance of each of these degradation processes in actual commercial cells is necessary towards providing device-scale technology

assessments and accelerating the development of hybrid electrochemical energy storage devices.

The combined approach of electrochemical and multi-modal characterization highlights the fact that commonly observed LIB degradation mechanisms of LMO and LTO are exacerbated in commercial LMO/AC//LTO/AC hybrid LIC cycled at high current. Correlations between the morphological parameters, crystallographic microstructure and chemical information along with electrochemical performance allow for a comprehensive understanding of the many processes contributing to the device failure. These aging mechanisms are visualized at different length scales in both electrodes, including their active materials and binders/conductive supports, and are accompanied with important degradation of the AC material as well. Morphological changes in the pore network structure of the electrodes and degradations gradients along the electrode thickness are reported to be the main contributing factors to the cell capacity fading.

2. Experimental

2.1 Electrode preparation and pouch cell assembly

The negative and positive electrodes consisted of $Li_4Ti_5O_{12}$ (EXM5034 from Johnson Matthey Battery Materials GmbH, LTO below) and $LiMn_2O_4$ (SLMO 03001 from Targray Technology International Inc., LMO below), respectively, as active materials. The conductive additive used in both electrodes was a mixture of Super P (SP_{Li}) carbon black powder (40 nm particle size), with a BET surface area of 62 $m^2\ g^{-1}$, according to the supplier's data, mixed with SFG6L graphite powder (5.5-7.5 μm particle size, BET surface area 17 $m^2\ g^{-1}$) obtained from Timcal®. Both electrodes also contained steam processed coconut shell activated carbon HDLC 20 BSTUW (115 F g^{-1}) from HAYCARB PLC® (BET surface area of 1800 $m^2\ g^{-1}$). The binder used was polyvinylidene fluoride (PVDF, Kynar HSV 900 from Arkema®). The electrodes were obtained from mixing 72%^{wt} of active material with 10%^{wt} of conductive

additive (6.4+3.6 $\%^{wt}$ of SP_{Li}+SFG6L), and 10%^{wt} of activated carbon with 8%^{wt} of PVDF in N-methyl-2-pyrrolidone (NMP). Preparation of slurry was carried out by mixing the components in a flask using a mechanical stirrer with a stainless-steel dispersing element. Electrodes slurries were applied on both sides of a current collector consisting of a modified Al foil 20 μm thick. Electrodes were dried for 24 hours at 150 °C under vacuum. The density and thickness of the pristine electrode (on one side) after drying are 1.46 g cm^{-3} and 55 μm for the negative, and 2.03 g cm^{-3} and 53 μm for the positive. The resulting loading of active material for the negative and positive electrodes are respectively 8 mg cm^{-2} and 11 mg cm^{-2}. Cross section images of the electrodes at their pristine state obtained by SEM are presented in the supplementary information (**Fig. S1**) along with their XRD powder pattern (**Fig. S2**).

LIC pouch cells were assembled in an Ar-filled glovebox by pairing 30 negative and 30 positive double-sided electrodes of □35 cm^2 interleaved with a porous insulating polyethylene separator (20 μm thickness, Lydall®). Electrode current collectors (modified Al foil of 20 μm thick) were welded to current leads made of Al foil of 500 μm thick. The balancing between positive and negative total capacity was around 1.04. The electrode pack obtained was sealed in a pouch shell made of laminated Al foil and impregnated with electrolyte. The electrolyte composition was as follows: a mixture of lithium bis(trifluoromethanesulfonyl)imide (LiTFSI) with $LiPF_6$ (98:2 in mass; 1.4 M total Li) dissolved in acetonitrile and propylene carbonate mixture (95:5 by volume) as a solvent. The electrochemical characteristics of these pouch cells, with rated capacity of 1.5 Ah (or up to 1.8 Ah at low current value) and mass of ca. 110 g, were studied by galvanostatic cycling on an Arbin BT-2000 test bench. The formation step of the pouch cell was constituted of: 1 cycle at 0.4 A (C/5); 2 cycles at 0.9 A (C/2); 3 cycles at 1.8 A (1C); 3 cycles at 5.0 A (3C); within a voltage range between 2.7 V and 1.35 V at room temperature. Subsequently, deep charge-discharge cycles at 15A (~10C) for aging were performed and the cells were discharged to the

OCV state of 2.47 V (SOC 70%), and calendar aged under ambient conditions for at least three months with periodical tests prior to disassembly and *post mortem* investigation along their desired cycle-life state.

2.2 Electrochemical measurements at electrode level

Prior to the stack dismounting, Electrochemical Impedance Spectroscopy (EIS) measurements have been performed in the stacks (□35 cm^2) in three electrodes configuration using a LFP reference electrode at different cycle-life state (BOL, MOL and EOL), while applying a small potential perturbation (5 mV) around the cell Open-Circuit-Voltage (OCV) with a frequency sweep from 200 kHz to 0.01 Hz (8 points/decade) at 25°C. Subsequently, cyclic voltammetry have been performed between 2.7 and 1.35V (1350 mV range) at different voltage sweep rates, estimated from the discharge duration of 3.2 min corresponding to a 19C current. The first vertex potential at 2.7 was hold 1 hour and the second at 1.35V for 10 min. Three passes have been made, respectively at 7, 0.7 and 0.07 mV/s. The positive and negative potentials are converted *vs.* Li^+/Li considering the LFP potential (3.424 V *vs.* Li). The voltage ranges were [1.35-2.7 V] for the cell, [1.3-2.5 V *vs.* Li] for the negative and [3.0-4.3 V *vs.* Li] for the positive electrode. To better understand electrode degradation, tortuosity measurements were performed on the electrodes recovered after formation and after ageing by using a previously described electrochemical method **[31,32]**. Detailed description is attached in the supplementary information document.

2.3 Sample preparation for X-ray investigation

Four different sets of samples were characterized by X-rays, corresponding to four different states of life of the electrodes. First, electrodes prior to cell assembly, labelled as the pristine state. Secondly, electrodes at their beginning of life state (BOL), *i.e.* after having followed the formation procedure described in the experimental section. Finally, electrodes that have deeply cycled according to the protocol described in the precedent

paragraph and reached their middle of life (MOL) or end of life (EOL). These latter conditions correspond either to capacity drop of respectively 10 (MOL) or 20 % (EOL), or internal resistance increase of 50 (MOL) or 100 % (EOL). These electrodes have been extracted from the middle of the full cell assembly. The dismantling of the cells was carried out in an Ar-filled glovebox, and the electrodes were washed by acetonitrile to remove lithium salt, and subsequently dried under vacuum over night. Samples of 250 μm diameter were extracted from the middle of the LTO and LMO electrode sheets (pristine or EOL state), using a dedicated chirurgical hole punch from Ted Pella Inc, inside an Ar-filled glovebox. The collected samples were subsequently fixed on top of individual glass capillary (200 μm diameter and 12.5 mm long) using UV acrylic glue. The glass capillaries were mounted on a brass sample holder for adequate mounting on the X-ray nano-tomography rotation stage. Identical samples were measured for both X-ray nano-tomography and X-ray diffraction characterization. Their capacity and resistance were monitored during cycling, and summarized in **Table S1**. In addition, larger samples (BOL, MOL or EOL) with section of 8×4 cm^2 have been selected for XPS analysis, whose capacity and internal resistance have been summarized in the supplementary **Table S1**.

2.4 X-ray nano-tomography

Acquisition-. X-ray nano-tomography acquisitions were performed on LTO/AC and LMO/AC electrodes at their pristine and EOL state at the ESRF ID16B beamline **[33]** using the holo-tomography technique **[34]**. Four tomographic scans were acquired using an incident X-ray beam with an energy of 29.2 keV and a flux of 2.6 10^{11} ph/s at four different sample-detector propagation distances. At each distance, 3203 projections, as well as 20 and 21 reference and dark images, were recorded on a PCO edge 5.5 camera (2560×2160 $pixels^2$) along a 360° rotation with an exposure time of 60 or 65 ms per step for the LTO and LMO electrode respectively. The total acquisition time was approximately 15 minutes per holo-

tomography scan. Acquisitions were performed at a voxel size of 25 and 50 nm, resulting in fields of view of respectively 64×54 μm^2 and 128×108 μm^2 for both representativeness and spatial resolution. 3D reconstructions were achieved in two steps: *(i)* phase retrieval calculation using an in-house developed octave script based on a Paganin-like approach using a delta/beta ratio of 233.6 for LTO and 142.6 for LMO, and *(ii)* filtered backprojection reconstruction using ESRF software PyHST2 **[35]**. Final volumes of 64×64×54 μm^3 (128×128×108 μm^3) with a voxel size of 25 nm (50 nm) in a 32 bit floating point were obtained.

Analysis-. In all cases, image analyses were performed on the entire reconstructed volume using the ImageJ software **[36]**. Qualitative analysis at the electrode scale was performed using the 50 nm voxel size images and quantitative analysis at the particle-scale and for tortuosity analyses have been done using the 25 nm voxel size images. Details on the procedures for the image segmentation and for their quantitative analyses (dimensional change of the electrode, volume fraction, size distribution and intra-connectivity of the segmented phases, crack growth) are presented in the supporting information (**Fig. S3**). The different phases (LTO, porosity and carbon) are segmented using thresholding on selected values, which were estimated from the deconvolution of the grey value histogram by the means of the multi-peak fitting tool of the OriginPro software. The AC, graphite and SP_{Li} materials are labelled in the same "carbon" phase, as they close by greyscale level are too close to be distinguishable. The tortuosity is estimated as following. First, the voxels in an initial seed plane are labelled with a distance of unity. A recurrent process then progressively labels the neighbouring voxels with their effective distance. The resulting voxel value is finally divided by the straight point-to-point distance (*i.e.*, y-position). The geometrical tortuosity has been calculated as the average of the tortuosity value along the electrode thickness. The efficiency of this method has been investigated in the case of $LiCoO_2$ positive

material, and shows dependency on the calculation method **[37]**. For our analysis, the results from quasi-Euclidean and city-block as the neighbouring definition have been averaged for each voxel to estimate the tortuosity of the pore phases.

2.5 X-ray diffraction

The same tomography samples affixed to glass capillaries were used without further preparation for X-ray diffraction. Measurements have been performed on the ID31 beamline (ESRF) with photon energy of 65 keV (0.1907Å), and the diffractograms were recorded with a Pilatus CdTe 2M detector approximately 2 m from the sample, calibrated using NIST SRM 674b CeO_2. The beam was focused to approximately 5 µm in the vertical direction, and scanned vertically through the electrode in grazing incidence geometry. Data were reduced using pyFAI **[38]** and Rietveld analysis was performed with the GSAS-II software package **[39]**.

2.6 X-ray photoelectron spectroscopy measurement

The XPS measurements were performed using a VersaProbe-II X-ray photelectron spectrometer from ULVAC-PHI with a micro-focused monochromated Al Kα X-ray radiation (1486.6 eV). Core level peaks spectra were recorded with a constant pass energy of 23.3 eV and 117.9 eV respectively, and under dual charge neutralization, for minimizing the differential surface charging effect that may occur at the surface of the electrode after cycling. Calibration of the spectra was done using the carbon C 1s peak at 284.8 eV related to carbon in the electrode binder.

XPS measurements have been performed on three different sets of electrodes complementary to X-ray tomography and diffraction analyses: electrodes at their beginning (BOL), middle (MOL) or end of life (EOL). The electrodes were transferred from the glove box filled with argon to the spectrometer using a dedicated transfer capsule to avoid sample oxidation under air exposure.

3. Results and discussion

3.1 Cycling performance and cell aging

After assembling the pouch cell according to the procedure detailed in the experimental section, a cycling formation procedure is applied: 1 cycle at 0.4 A (C/5); 2 cycles at 0.9 A (C/2); 3 cycles at 1.8 A (1C); 3 cycles at 5.0 A (3C); within a voltage range between 2.7 V and 1.35 V. **Fig. 1a** illustrates the charge-discharge curves for the first 4 cycles of this formation process for the studied cell, and **Fig. 1b** shows the capacity and coulombic efficiency of the cell during the entire formation process. Typically, the initial capacity measured is around 1.85 A.h with a coulombic efficiency of 92% (C/5) and then steadily decreases to 1.67, 1.6 and 1.45 A.h while C-rate increases (C/2, 1C and 3C respectively), corresponding to relative capacity drop of □10 %, □15 % and □20 % respectively. Nevertheless, the final cycle of each C-rate step presents a high coulombic efficiency close to 99%. Additionally, the incremental capacity curves (dQ/dV) of these formation cycles are presented in the **Fig. 1c**, which reflect the sum of processes that occur at the positive (LMO) and negative (LTO) electrodes. Both peaks observed are characteristic of the two-step redox process of the Mn^{4+}/Mn^{3+} couple **[40,41]**, corresponding to both plateaus [2.4-2.5] V and [2.6-2.7] V observed on the cycling curves of the **Fig. 1a**. Although the peak intensity is progressively reduced when the C-rate value increases, the potential values barely change, witnessing thus only a slight decrease of the redox couple activity without a tremendous polarization effect. Following the electrochemical formation procedure, two LIC pouch cells were deeply cycled at high C-rate (10C). The initial characteristics (BOL) measured in the early cycle-life, *i.e.* after the formation step procedure were: 1.4 (1.5) Ah of capacity and 0.9 (0.9) mOhm of direct current (DC) resistance for the electrode cycled until MOL (and EOL respectively). The **Fig. 2a** presents the charge (solid)/discharge (dash) curves of the analyzed

electrode at the BOL, MOL and EOL state at C/3. During the cell aging, the capacity has dropped to 1.2 A.h (MOL) and 0.8 A.h (BOL) after 500 cycles, corresponding to relative capacity decreases of nearly 15 and 45 % respectively. The values are summarized in the **Table S1**. The **Fig. 2b** displays the respective incremental capacity curves for the studied cycle-life states. The redox peaks at 2.45 and 2.57 V show a linear decrease in terms of activity along aging, which might be indicative of loss of lithium inventory along cycling. This could be related to irreversible Li^+ consumption through Solid Electrolyte Interface (SEI) and/or Cathode Electrolyte Interface (CEI) formation through side reactions at the negative/positive, and/or progressive active material disconnection along cycling. In the meantime, the peak position is shifting towards higher potential in oxidation (2.45→2.49 V / 2.57→2.63 V) and reciprocally lower potential in reduction (2.42→2.38 V / 2.56→2.52 V), which is well correlated with the stack internal resistance increase (measured by DC measurement) from 0.9 (BOL) to 1.2 (MOL) and 1.4 mOhm (EOL) (see **Table S1**). These peak shifts lead also to a steadily decreasing symmetry of the redox peaks, highlighting thus the loss of reversibility of the system. EIS characterization was performed at the BOL and EOL states on these cells as presented for the complete cell, negative and positive electrodes in the **Fig. 2c**, **2d** and **2e** respectively. Enclosed close-up views are included for high-medium frequency domain visibility. From the measurements it appears that, some interfacial changes are clearly visible from the BOL to the EOL state. The ohmic resistance of the cell R_{HF}^{cell}, measured at the intersection with the real axis and corresponding to the sum of the resistances of current collectors, active material, electrolyte and separator, is increasing with cycling (**Fig. 2c**) from 17.5 to 24 mΩ. By analyzing the respective contributions of the negative and positive sides, it is clear that this increase is mainly related to changes visible on both sides (**Fig. 2d**, **2e**) in terms of R_{HF} increase, with a slightly larger contribution from the negative one (+25 % relative increase *vs* +21 %). This increase could be associated with electrolyte

resistance thanks to possible gas formation, partial electrode disconnection, and thus higher polarization. In addition, the increase of the medium frequency depressed semicircle for the negative side with cycling reflects the increase of the resistance of the electrode due to the interfacial layer formation (SEI). This SEI build up and associated impedance increase is accompanied with a relative increase in charge transfer resistance R_{ct}, as depicted by the magnitude increase of the second depressed semicircle (10 – 1Hz range) at the negative electrode side, which support the hypothesis of particle/particle and/or electrode/current collector disconnections. On the counter positive electrode, a small but detectable possibly new contribution is highlighted by the appearance of a lower resistive high-frequency (1kHz-500 Hz) semi-circle at the EOL state. This could reflect a new capacitive effect due to the formation of new particle/particle interfaces and/or Cathode Electrolyte Interface (CEI) layer. Taken altogether, the main changes observed at the cell level originated from resistive passivation layer formation at both the negative and positive electrode along aging, along with charge transfer increase due to particle or electrode disconnection at the negative.

In order to decipher the role of each electrode toward the global electrochemical performance decay, cyclic voltammetry (CV) at different voltage sweep rates have been performed in a three electrode configuration using a LFP reference electrode at different cycle-life state (BOL, MOL and EOL). The results are presented for the complete cell (**Fig. 3a**) and for the negative (**Fig. 3b**) and positive (**Fig. 3c**) electrodes, which potentials are converted *vs* Li^+/Li considering the LFP potential (3.424 V *vs.* Li), and sweep rates values increasing from 0.07 (left) to 7 mV/s (right). At low voltage sweep rate, we can consider that LTO and LMO active materials, at the negative and positive electrode respectively, contribute mainly to the electrochemical response (**Fig. 3b** and **3c**). Peak shifts correlated with aging are observed at the negative electrode at low sweep rates, which likely indicates a resistive passivation of the active material surface leading to a higher polarization. Cut-off voltages are

also shifting for negative and positive upon aging, but all the peaks associated to redox process are still in place, indicating that all the active material which remains accessible at EOL is working. Peak areas, *i.e.* the corresponding amount of reaction with accessible materials, are decreasing along cycling in the case of both positive and negative electrodes and losses are estimated around -30% and -20% respectively (at 0.07mV/s), implying possible irreversible loss of active material due to disconnections or pores clogging. As losses of active material are on the same order of magnitude on both sides at EOL, it could be assumed that gas pockets are formed or pores are clogged upon aging, disabling part of the (de)lithiation of positive and negative materials at the same time. As expected, at high sweep rates the electrochemistry is dominated by the fast capacitive response of the activated carbon *vs.* the comparatively sluggish LTO/LMO. The CV curves for both electrodes are strongly distorted at high sweep rate with aging, which could indicate that the activated carbon is also damaged or has become clogged in both electrodes, thus contributing to the capacity decay at the EOL state. However, the less intense peaks of LTO/LMO present also a decreasing intensity upon aging, their damaging are still visible at high C-rate. It is interesting to underline that barely no changes in the AC response are visible between BOL and EOL states, which could indicate that pore clogging occurred during the formation step of the pack and no further degradations are observed. Additional C-rate measurements presented in the supplementary information (see **Fig. S4**) shows that LMO limits charge storage at low C-rate after aging, which might indicate a more pronounced degradation of the active material compared to LTO/AC electrodes. In total, the larger irreversible capacity loss measured at the positive is roughly accounting for a half of the capacity fade reported.

3.2 Morphological evolution

In order to investigate in more details the degradation process of the hybrid LIC pouch cell, representative samples have been selected for post mortem analysis after reaching the

desired cycle-life state (MOL, EOL) in comparison to the pristine state. The cells were discharged to the OCV state of 2.47 V (SOC 70%) and calendar aged under ambient conditions for at least three months with periodical tests prior to disassembly at SOC 0%.

3.2.1 Electrode-scale level

2D sections extracted from the X-ray nano-tomography volumes reconstructed within the negative LTO/AC electrodes are presented in **Figure 4a** and **4b** for the pristine and EOL states respectively. The top images correspond to transversal sections, across the thickness of the electrodes, while below are the in-plane cross-sections selected at different heights through the electrode, as indicated by the dashed lines ($b_{1\rightarrow3}$). Initially, the as-prepared electrode presents a homogeneous microstructure along its thickness with well-dispersed and small LTO particles, and large AC particles (see also **Fig. S1a**). Whereas at the pristine state the electrode film / Al current collector interface does not show any delamination and/or cracks that would lead to electronic disconnection, the EOL electrode presents clear signs of delamination as indicated in **Fig. 4b** by the significant crack formed near the current collector. That is consistent with the increase of the first semi-loop observed at high frequency in EIS spectra. Locally, this crack occupies at least $10\%^{surf}$ of the examined in-plane cross section, as depicted on the red labelled image, corresponding to the red dashed line (b_3) on the cross sectional image of **Fig. 4b**. Moreover, on the top surface which contacts the separator, major cracks and disconnections are visible both on the cross section image and on the in-plane one below (green dashed line b_1 **Fig. 4b**). These cracks represent locally $8\%^{surf}$ of the image section and nearly $4\ \%^{vol}$ of the electrode top surface sub-volume. The forms and positions of the bubble-like cracks suggest that they might be related to important gas release, occurring at the LTO particle surface **[28]**, which subsequently induces active material disconnections, hence capacity fade and internal resistance increase as evidenced in **Fig. 2a** and **2c** respectively. Despite the fact that acetonitrile solvent helps mitigating the gas release in LTO

negatives **[42]**, this generation could be exacerbated at high C-rate long cycling in LTO/AC negative **[26, 43]**. Following the same display format as for **Fig. 4a** and **4b**, the **Fig. 4c** and 4**d** present 2D images extracted from reconstructed volumes within the LMO/AC positive electrode at the pristine and EOL state respectively. Interestingly, the LMO/AC electrode at the EOL state seems to present no evident macro-morphological degradation signs unlike the LTO/AC one, which is in agreement with the electrochemical analysis carried out, reflecting major degradation at the negative side. While no obvious qualitative changes can be directly appreciated in the reconstructed images at this magnification, a more quantitative analysis, gives deeper insights about porosity changes within the electrodes.

The **Figure 4e** presents the porosity values for the negative and positive electrode at their respective pristine and EOL state obtained after image segmentation. The corresponding pore size distribution curves expressed in terms of cumulated volume fraction are displayed jointly (**Fig 4f)**. At the pristine state, the porosity measured for the LTO/AC and LMO/AC electrodes (50.8 % and 37.2 % respectively) are close to the theoretical values of the electrodes (52.2 % and 42.6 % respectively) estimated from their respective active material loadings *lo*, thicknesses *e* and densities d_{th} according to the formula:

$$\varepsilon = 100.\left(1 - d_{th}/d_{exp}\right) = 100.\left(1 - d_{th}.e/lo\right) \quad (1)$$

The slight differences between theoretical and experimental values are most probably due to incertitude for estimated the porosity in the binder/PVDF phase with the limited spatial resolution (voxel size of 50 nm). This difference is then exacerbated for the positive electrode, where the “carbon” domain are larger compared to the negative electrode. Both negative and positive electrodes have different porous network structure, in terms of total volume fraction and pore size distribution with respective initial median size of 0.26 and 0.88 µm. At the EOL state, a general shrinkage of their networks is measured, with median pore size relative

decrease of -35 and -25 %, along with a global reduction of their pore volume fraction, -5 % and -8 % for the negative and positive electrode respectively (**Fig. 4e**-**f**). This shrinkage have more detrimental impact on the negative electrode porous network as it is initially composed of smaller pores, as supported by the EIS data (**Fig. 2d**). The reduction of the pore phase is accompanied with a respective increase of the volume of carbon phase fraction, +5 and 6 % for negative and positive electrode respectively, while the active material fraction stays practically steady. The volume expansion of this phase, initially containing the conductive additive and activated carbon, is most probably associated with electrolyte degradation products, which has the same grey scale level as the other carbon-based materials of the electrode,. The fact, that the porosity structure narrowing is more intense at the negative electrode, could be correlated to its higher contribution to the total R_{HF} and R_{SEI} increase after aging, as supported by the EIS data (**Fig. 2c**-**e**). In the meantime, a similar layer formation has been observed in the present case on *post mortem* SEM analysis of the EOL state of LMO electrode, which present a darker covering layer at the particles surface (see supplemental information **Fig. S6a** and **S6b**). XPS analysis carried on the positive electrode samples (BOL, MOL and EOL), showed the increase of the O (CEI) related peak at a binding energy of 513.5 eV observed in the O 1s peak core level, while the peak associated with the O^{2-} of LMO is decreasing (**Fig. S6c**). This highlights the formation and growth of a layer composed of organic species on top of the LMO active material particles. The contribution of this layer formation toward the actual loss of electrochemical performance is however limited compared to the negative electrode (**Fig. 2d** and **2e**).

The determination of the tortuosity of the electrode pore network allows quantifying the change in the electrode conductivity through the Li^+ ions diffusion in the electrolyte. The geometrical values of the tortuosity have been estimated from averaging results of quasi-Euclidean and city-block model as neighbouring definition for each voxel of the pore phase of

each electrode (**Fig. 5**). The higher initial average tortuosity value of 1.46 measured for the negative electrode is associated with the five times narrower pore channels of the more constrained LTO/AC electrode porosity (particle size and compactness), compared to 1.26 for the positive electrode. Therefore, the 3D mappings are represented with slightly different color-scale to highlight the heterogeneities at the electrode scale. The color-scale corresponds to the geometrical tortuosity factor expressed as the ratio of the actual path length over the straight-line estimated along the electrode volume for the negative electrode at the pristine and EOL state (**Fig. 5a**), and for the positive electrode (**Fig. 5b**). Some 2D transversal slices have been added below each 3D volume for a more comprehensive analysis, displaying high heterogeneities and gradients across the electrodes' volume. The planes' heights have been kept constant for the sake of comparison. At the negative, the pore channels shrinkage reported after aging leads to a large increase of the average tortuosity value (1.74), with a more uniform profile in 3D, highlighting a more homogeneous morphological change on this side. Moreover, tortuosity of the pore network is increased already near the current collector at the EOL state. On the counter side, only a slight average increase can be reported on the positive electrode (1.26 *vs.* 1.34). Heterogeneities at the electrode's volume appears more marked for the positive. This gradient tends to be more pronounced and more heterogeneous across the electrode thickness at the EOL state mostly for the positive electrode (**Fig. 5b**) and also across the in-plane section. This changes could amplify the heterogeneities in the degradation of LMO particles, as observed at the particle scale. In the meantime, tortuosity estimation have also been done using the complementary EIS spectra in symmetric cells in blocking condition (see complementary information and **Fig. S5**) and the calculation method proposed by Johannes Landesfeind *et al*. **[31]** following the equation:

$$\tau = \varepsilon \frac{R_{ion}.A.\kappa}{2e} \quad (2)$$

where ε is the electrode porosity, e its thickness and A its surface, R_{ion} the ionic resistance and κ the electrolyte conductivity. These calculations are valid provided the charge transfer resistance is negligible compared to the ionic one. In the present case, the electrolyte conductivity is around 8.85 mS/cm and the LTO(LMO)/AC electronic conductivity is in the order of magnitude of S/cm resulting in a ratio of $R_{ct}/R_{ion} < 10^{-2}$. However, possible degradation after aging could have affected the electrode leading to less blocking conditions at the electrode, as visualized for EOL state EIS spectra with less vertical profile (especially on the positive electrode side). The obtained values are summarized in **Table S2**. At the EOL state, the EIS-based values have been estimated using the corrected electrode porosity from the tomography measurements rather than the theoretical values. It appears that the EIS-based values are higher than the geometrical ones (especially for the LMO/AC electrodes). Globally, a noticeable increase of the average tortuosity of the pore network after aging is visible in both electrodes using either the geometric or the electrochemical estimation. The difference between these values, especially at the EOL state, is attributed to the dissolution of the electrolyte decomposition products through the washing process applied before *post-mortem* investigation. In fact, the SEI/CEI layers play a major role in increasing the average tortuosity of the pore network thanks to a highly nano-porous morphology, which is drastically increasing the mean shorter distances. It is possible to predicate that the geometrical method for tortuosity determination allows quantifying the impact of the morphological changes on the porous network structure (at a given spatial resolution), without considering its chemical changes that could only be evaluated thanks to the EIS based method. The combination of both methods helps discriminating the contribution of both aging mechanisms on the average electrode evolution. The increased tortuosity at the EOL state for both electrodes will consequently result in higher resistivity pathways for ionic conduction and thus lower capacity of the active material, leading to shorter cycles (**Fig. 2a** and **2c**). In

summary, porosity volume reduction and shrinkage along with tortuosity increase, are the most important morphological changes at the electrode scale level. Additionally, the high heterogeneity in the accessibility of the pores should induce disparity in the activity of the active material and thus lead to degradation gradients at the electrode scale. This will be presented in more details in the following section.

3.2.2 Particle-scale level

Figure 6 presents the active materials particle changes and size distributions evolutions during aging, respectively LTO (**Fig. 6a-c**), LMO (**Fig. 6d-f**) and AC (**Fig. 6g-i**). The particle sizes are estimated from segmented 3D reconstructed volumes with a pixel size of 25 nm using a local thickness measurement **[44]**. The local thickness calculation has a stochastic error of ± one voxel. The precision of this estimation depends thus mostly on the image segmentation quality and spatial resolution (see **Fig. S3** for detailed procedure). Although, electrochemical data of the section 3.1, which have shown important degradation of LTO/LMO and AC materials with probably disconnections and/or pores clogging, tomography images bring to light clear complementary information about these degradations.

On the negative electrode, slight changes are visible on the local thickness distribution of the LTO particles with a relative variation of the median size of -25% from 0.32 to 0.24 μm (**Fig. 6c**). The LTO active material is present as well dispersed particles along the electrode matrix with local aggregates composed of sub-micrometric particles and rare large chunks of active material. The internal porosity of these aggregates increases after aging (**Fig. 6a-b**). In fact, along the overall electrode volume analyzed, the large LTO aggregates show a mean inner porosity value of 11.6 (±1.5)% at the pristine state, and 24.7 (±2.7)% at the EOL state, corresponding to an important relative increase of more than 100% (measurement done on tens of aggregates). This porosity formation is observed on multiple LTO large aggregates spread along the entire electrode, whereas some rare large chunks of active material, which

appear dense at the pristine state, does not suffer disaggregation and/or porosification (third particle from the left on **Fig. 6b**). Different assumptions can be proposed to explain the porosity increase of the active material agglomerates:

(i) The active material corrosion could lead to further dispersion of the aggregates. The inhomogeneity of these degradations are mostly associated with the percolation path of the electrode, which is highly dependent on the carbon phase dispersion (carbon black and activated carbon) and C-rate **[45]**.

(ii) The side products of the electrolyte degradation (SEI and gas release) in these active material aggregates may also promote particle disconnection **[28]** and consequently porosity increase, especially when gas release is promoted at high C-rate and after long cycling conditions **[43]**.

(iii) The binder resiliency after repetitive lithiation/delithiation cycle at high C-rate might not be able to efficiently keep the LTO aggregates from dispersing **[20]**.

On the positive electrode, cracking of the LMO particles after aging is evidenced by the images of the **Fig. 6d-e**. It can be visualized through the general shift toward smaller particle size between the pristine and EOL state (**Fig. 6f**) and important reduction of the median size from 17 to 4 μm (-76% relative variation). This phenomena must have been exacerbated under the repetitive cycle of lithiation/delithiation at high C-rate along with the low discharge cut-off voltage of 3 V *vs* Li^+/Li at the positive, as also reported in the literature **[46,47]**. In addition, some of the LMO particles show an intense porosification at the EOL state (third particle from the left on **Fig. 6e)**, leading to the formation of small sub-micrometric particles as highlighted on the left tail of the particle size distribution at the EOL state (**Fig. 6f**). It is also important to note that some LMO particles, although few, present already a cleaved structure initially, which could have originated from the slight breaking of primary active material particles during the planetary mixing process used for slurry preparation and

homogenization. The close up views of AC particles in the **Fig. 6g-h** show the evolution from porous at the pristine state, to partially cracked particles at the EOL state. This phenomenon is reported on both the negative (left) and positive (right) electrode side. The identifiable cracking pattern is particularly highlighted thanks to phase contrast imaging. Because of this particle cracking, the median size of the AC particles is decreasing from 6.7 (7.9) to 4.76 (4.73) μm at the negative and positive electrode side respectively from the pristine to the EOL state (**Fig. 6i**), which indicate parallel degradation in the LIC system. The disconnection through cracking of AC particle is thereby reducing the overall capacitance of the system, with important limitation at high current solicitation for the LIC hybrid system. These AC particles presents inner pores with a size ranging from 1.34 to 8-10 nm (see supplementary **Fig. S7**), which are not accessible with nano-tomography at 25 nm. However, it is our belief that pore clogging occurring at a very small scale plays an important role on the capacitance reduction of the material as well. In order to quantify the homogeneity/heterogeneity of the active materials (LTO, LMO, AC) degradations, **Figure 7** displays the relative disaggregate/crack fraction in the active material, noted d_{defect}, as a function of the distance from the current collector. For each slice in the reconstructed volume, a density of defects is calculated as the ratio of number of detected defects over the fraction of active material in the slice, *i.e.* LTO and AC for the negative (**Fig. 7a** and **7c**) and LMO and AC for the positive electrode (**Fig. 7b** and **7d**):

$$d_{defect} = \frac{N^{defect}}{N_{AM}} \times 100 \quad (4)$$

with N^{defect} and N_{AM} the number of pixels corresponding to defect or active material respectively. The same analyses have been performed for in-plane directions and do not highlight important or indicative heterogeneities.

First, it appears clearly that the average volume of defects are increasing after long-term aging, independently of the active material considered for both the positive and negative

electrode, as qualitatively observed already on the images of **Figure 6**. The average disaggregation per LTO aggregate is more than doubled after EOL compared to the pristine state, while the mean crack fraction of LMO particles is five times higher at EOL. These degradations appear to be homogeneously increasing in the case of the negative electrode, for both AC and LTO (**Fig. 7a** and **7c**), whereas it is rather irregularly evolving in the case of the positive electrode (**Fig. 7b** and **7d**). In fact, the disaggregation of the LTO active material and AC particle cracking are visible over a large part of the negative electrode thickness with slightly higher values near the separator/electrode interface for the LTO disaggregation. This result can be expected, considering the high rate capabilities of the LTO/AC material **[3]**. On the opposite, an important gradient of degradation is revealed across the positive electrode for the LMO particles. The upper half of the electrode presents increased crack fraction up to a factor of two, compared to the LMO particles closer to the current collector (**Fig. 7b**). In the regions where the degradations are rather more visible on the LIB active materials, a less intense use of the AC particles is observed provided LMO/LTO participate to the power response of the LIC system. Consequently, the AC cracking appears more severe at the positive electrode side, and especially near the lower part of the electrode's thickness, where interestingly LMO particles' cracking is less pronounced. This is consistent with the previous electrochemical observations displaying higher degradation of the AC at the positive electrode (**Fig. 3b** and **3c**). The heterogeneity of these active material degradations at the electrode level could be associated with the increase in tortuosity of the pore network between the pristine and EOL states as reported on **Fig. 5a** and **5b**. The gradient of lithium diffusion and heterogeneity across the electrode thicknesses are leading to localized uneven utilization of the active material, consequently resulting in non-homogeneous particle aging at the electrode scale.

3.3 Atomic-scale evolution

In order to get more insights about Li ions inventory loss and degradation at the atomic-scale, complementary XRD and XPS measurements have been performed on the samples at their respective aging states. Rietveld analysis of the pristine and EOL electrodes was performed, to compare with more insights the microstructural evolution of the LMO and LTO (**Fig. 8**). Slight amorphous contribution from carbon/polymer at low angle are visible and do not present major changes after aging. A small but detectable lattice contraction of the LTO between 8.3614 and 8.3604 Å was detected (**Fig. 8a**), in contrast with the small lattice expansion reported previously using lower resolution diffraction **[17,48]**. Nonetheless, this was surprising considering the fact that only a very low lattice parameter variation of 0.006 Å upon the two first cycles of the material has been reported previously in the literature by F. Ronci *et al.* **[17]**. The reflections of the EOL material were significantly broadened versus the pristine material for both the LMO and LTO phases (**Fig. 8a** and **8b**). Line broadening arises principally from the finite crystallite size of these materials, and distortion of the lattice caused by crystal defects and grain boundaries, known collectively as microstrain. These contributions can be decoupled through their different angular dependence. An example of the increased peak broadening observed for the LMO after aging is shown in **Fig. 8b**. The crystallite size and micro-strain estimated for the pristine and EOL samples are summarized in **Table S3**. The mean crystallite size of the LMO decreases by 51% after aging, while the LTO decreases by 25%. This is consistent with the cracking, corrosion, disaggregation, and pulverization phenomena observed with X-ray nano-tomography in both electrodes. Not only are the secondary aggregates broken up, but the primary crystallites are also significantly fractured, leading to further degradation and SEI growth. The reduction of the crystallite size could also be associated with Mn dissolution, which has been well reported for LIBS systems in the literature **[24,29,30]**. In the present case, a pronounced surface roughening of the LMO active particles has been observed and measured (on two isolated particles), as presented in

the supplementary information (**Fig. S8**), revealing the dissolution of the particles and/or growth of a cathode electrolyte interface (CEI).

Unlike previous studies **[49]**, the microstrain for the LTO decreases, and we do not observe any significant disordering of the LTO after cycling, which we attribute to the comparatively larger surface area to crystallite volume of this particular material. Unfortunately, microstrain from powder diffraction cannot distinguish between inter- and intra- particle heterogeneity in lattice parameter. The microstrain for the LMO increases significantly by the end of life. Increases in microstrain are characteristic of stacking faults, dislocations, defects, and structural disorder caused by particle cracking, which is consistent with the morphology of the aged LMO particles. The microstrain measured for the LMO particles in this work is ten times higher compared to values previously reported on LMO aged at lower C-rate (C/5) **[50]**, which indicates that the aging mechanisms of the primary particles are accelerated by rapid (dis)charging. For intercalation materials like LMO and LTO, microstrain can simply reflect a distribution in the electrode's state of charge, caused by partial electrochemical disconnection over time. Disconnected particles adopt different lithiation states than electrically connected ones after cycling. This relies on the percolation pathway in the electrode and heterogeneities tends to arise when considering large currents applied during short intervals, counteracting the homogenization of charge and potential over the electrode **[45]**. If this distribution persists after cell disassembly and exposure to air, then single-particle techniques are necessary to differentiate inter- and intra-particle aging phenomena.

Complementary XPS analyses performed on negative (**Fig. 9a**) and positive (**Fig. 9b**) electrodes at different cycle life states (BOL, MOL and EOL) show the presence of manganese at the surface of the negative as early as the middle of life state and its increase along cycling, as depicted by the peak intensity rising at a binding energy position of 641.7 eV, while a decrease is measured on the positive side. Even so, the formal oxidation state of

manganese cannot be elucidated, the Mn $2p_{3/2}$ peak asymmetry and binding energy position, may indicate that manganese is deposited on the negative electrode surface through organometallic species. Similarly, Vissers *et al.* **[51]** proposed that the manganese ions in the electrolyte react with one or more of the primary constituents of the inner inorganic SEI layer, namely Li_2CO_3, LiF, and Li_2O. Moreover, this covering appears to be non homogeneous and rather thin, considering the fact that the Ti $2p_{3/2\text{-}1/2}$ core level peaks (**Fig. 9c**) are still visible at every state of health and that the depth probe used during the measurements is of ~5-10 nm with a X-ray size spot of ~100 μm^2. On the counter side, the decrease in peak intensity of manganese in its formal oxidation state +IV may indicate its dissolution but also CEI deposition on the surface of the LMO active material, as indicated by the rising evolution of the F 1s core level peak intensity at 684.7 eV during cycling (**Fig. 9d**). The CEI layer growth is in accordance with the observation of a thin deposited layer at the surface of LMO particles. This CEI layer is mostly composed of inorganic species, as indicated by the increase in the peak corresponding to LiF species (**Fig. 9d**), along with some organic carboxyl species (**Fig. S4c**), contributing towards lithium inventory loss previously postulated by the linear decrease of the peak intensity reported on the incremental capacity curves of **Fig. 2b** and **Fig. 3b-c**. However, the determination of the exact composition of this CEI layer remains out of the scope of this paper. In addition, the pore/graphite areas near LMO particles present shifts in the image grey values between the pristine and EOL states, which may indicate possible changes in the chemical composition of these regions (see supplemental information on **Fig. S5)**. One explanation could be that charge trapping is favored due to insulating CEI in these regions. Another possible explanation lies in the eventual re-deposition of the Mn species on the LMO electrode surface along with electrolyte decomposition products as previously reported **[39]**. Anyhow, this reduction layer formation should induce cell polarization increase leading to further capacity decay, which could be exacerbated at high C-rate as also evidenced

by the shifts in the electrochemical peaks of the incremental capacity curves of **Fig. 2b**. In addition, these changes confirm that aging occurs at the nanocrystallite level, in addition to any larger, morphological changes such as gas formation and SEI/CEI layer growth, leading to electrode film cracking and delamination. The microdiffraction data for both electrodes at EOL do not show new peaks corresponding to irreversible phase transformation of either active material, or newly deposited crystalline phases, in agreement with previous work **[48,49]**. However, the spectroscopy analyses show clear signs of manganese dissolution/deposition from the positive that accentuate along with cell aging. The later one is deposited on the LTO/AC negative surface through inorganic species, which are mainly amorphous. Hence, this active material inventory loss is drastically limiting the cycle-life of the cell.

4. Conclusion

The combination of electrochemical assessment and X-ray characterization tools elucidates the degradation mechanisms of a LIC hybrid cell at multiple length scales with high precision. This has been studied with the exemplary case of the LTO/AC//LMO/AC parallel hybrid full cell, using a commercial stack configuration and providing thus useful insights in the failure causes. The significant degradation in the microstructure of the different active materials supports the hypothesis that aging phenomena at both the negative and positive electrodes of these cells are responsible for the performance losses measured along cycling tests. These degradations are jointly occurring at different length scales, *i.e.* the electrodes, secondary/primary particles and crystallites/atoms.

(i) At the electrode level, the porous network shrinkage along with its tortuosity increase, at both the negative and positive electrode, is leading to higher

polarization of the cell and consequently shorten cycle- life when cycling at very high current. This has been attributed to the growth of a decomposition layer formed from electrolyte reduction revealed through EIS measurements along with AC particle pulverization. The role of a coating layer associated with an adequate polymer binder can be crucial for promoting the LTO/AC electrode mechanical integrity while mitigating the risk of delamination and or cracking (better anchorage of the binder to the active material and current collector), and also for decreasing the amount of gas released as well.

(ii) At the particle scale, active material cracking is reported for the AC and LMO along with substantial disaggregation of the LTO aggregates disaggregation resulting from slight corrosion measured at the crystallite scale, and/or SEI formation. Important gradients of degradations have been measured at the positive electrode, where the LMO cracking is twice more pronounced close to the separator/electrode interface compared to close to the current collector. The high current solicitations appear more detrimental to the LMO/AC material.

(iii) At the atomic scale, the significant accumulation of micro-deformations inside crystals, and the large reduction of the LMO crystallite size has been observed and quantified leading to severe and heterogeneous cracking of active particles limiting therefore the cell's cycle-life. It is accompanied with dissolution of Mn species and subsequent precipitation on the negative electrode surface in form of reduced species through repetitive cycles of charge/discharge at high C-rate. This dissolution is mostly present on the positive electrode surface and could also promote the LMO particle cracking, underlining thus the importance of preventing Mn^{3+} dissolution from the LMO cathode material.

In global, the irreversible lithium inventory loss related to SEI/CEI formation, Mn dissolution and particle cracking/disconnection are reported to be the main contributing factors to the cell capacity fading and are counting for approximately a half of the total capacity loss. The rest is due to morphological changes in the pore network structure of the electrodes and degradations gradients along the electrode thickness, leading to polarization increase and preferential degradation at the electrode/separator interface. This showcases the importance of both cathode and anode active materials in the capacity fade mechanism, and the relevance of characterizing full devices for further understanding of aging phenomena.

Acknowledgements

The authors thank the European Union's Horizon 2020 research and innovation programme (Grant agreement No 814106, TEESMAT project). The ESRF is thanked *for provision of synchrotron radiation facilities (in-house beamtime at ID16B and ID31) as well as t*he PFNC CEA Minatec for instrumentation access. A special thank to E. T. Capria and T. Schulli from the ESRF, and Y. Butkov from Yunasko-Ukraine LLC, for their dedication to the project and collaboration.

Reference

[1] R. Schmuch, R. Wagner, G. Hörpel, T. Placke, M. Winter, Performance and cost of materials for lithium-based rechargeable automotive batteries, Nat. Energy 3 (2018) 267–278.

[2] M. Armand, P. Axmann, D. Bresser, M. Copley, K. Edström, C. Ekberg, D. Guyomard, B. Lestriez, P. Novak, M. Petranikova, W. Porcher, S. Trabesinger, M. Wohlfahrt-Mehrens, H. Zhang, Lithium-ion batteries – Current state of the art and anticipated developments, J. Power Sources 479 (2020) 228708.

[3] G.G. Amatucci, F. Badway, A. Du Pasquier, T. Zheng, An asymmetric hybrid nonaqueous energy storage cell, J. Electrochem. Soc. 148 (2001) A930-A939.

[4] A.D. Pasquier, I. Plitz, S. Menocal, G. Amatucci, A comparative study of Li-ion battery, supercapacitor and nonaqueous asymmetric hybrid devices for automotive applications. J. Power Sources 115 (2003) 171–178.

[5] A. Du Pasquier, I. Plitz, J. Gural, F. Badway, G. Amatucci, Power-ion battery: Bridging the gap between Li-ion and supercapacitor chemistries. J. Power Sources 136 (2004) 160–170.

[6] D. Cericola, P. Novák, A. Wokaun, R. Kötz, Hybridization of electrochemical capacitors and rechargeable batteries: An experimental analysis of the different possible approaches utilizing activated carbon, Li4Ti5O12 and LiMn2O4, J. Power Sources 196 (2011) 10305-10313.

[7] H. Zhou, M. Liu, H. Gao, D. Hou, C. Yu, C. Liu, D. Zhang, J.-C. Wu, J. Yang, D. Chen, Dense integration of solvent-free electrodes for Li-ion supercabattery with boosted low temperature performance, J. Power Sources 473 (2020) 228553.

[8] D. Cericola and R. Kotz, Hybridization of rechargeable batteries and electrochemical capacitors: Principles and limits, *Electrochim. Acta* 72 (2012) 1-17.

[9] F. Beguin and E. Frackowiak, Supercapacitors: Materials, Systems, and Applications, Wiley-VCH, Weinheim (2013).

[10] A. B. Stepanov, I. N. Varakin, V. V. Menukhov, and A. D. Klementov, *Double Layer Capacitor*, Patent US 6181546, Publ. 2001

[11] Y. A. Maletin, N. G. Stryzhakova, S. O. Zelinskyi, S. I. Chernukhin, Energy Storage Technologies Based on Electrochemical Double Layer Capacitors: A Review. Theor Exp Chem 57 (2021) 311–324.

[12] A. Yahalom, Y. Dahan, V. Prihodko, M. Averbukh, Experimental verification of internal resistance and capacitance of CPQ2300S Li-ion ultracapacitors (JSR Co.), IEEE Intern. Conf. on the Science of Electrical Engineering (2016).

[13] W. J. Cao and J. P. Zheng, *Proc. 22nd Intern. Seminar on Double Layer Capacitors and Hybrid Energy Storage Devices*, Deerfield Beach, FL, 99-105 (2012).

[14] S. Chernukhin, D. Tretyakov, and Y. Maletin, *Hybrid Electrochemical Energy Storage Device*, Patent US 2014/0085773 A1, Publ. 2014.

[15] L. Ping, J. Zheng, Z. Shi, J. Qi, C. Wang, Electrochemical performance of MCMB/(AC+LiFePO4) lithium-ion capacitors, Chin. Sci. Bull. 58 (2013) 689-695.

[16] X. Hu, Z. Deng, J. Suo, Z. Pan, A high rate, high capacity and long life(LiMn2O4|AC)/Li4Ti5O12 hybrid battery-supercapacitor, J. Power Sources 187 (2009) 635-639.

[17] F. Ronci, P. Reale, B. Scrosati, S. Panero, V. Rossi Albertini, P. Perfetti, M. di Michiel, J. M. Merino, High-Resolution In-Situ Structural Measurements of the Li4/3Ti5/3O4 “Zero-strain” Insertion, Material. J. Phys. Chem. B 106 (2002) 3082−3086.

[18] A. Guerfi, S. Sévigny, M. Lagacé, P. Hovington, K. Kinoshita, K. Zaghib, Nano-particle Li4Ti5O12 spinel as electrode for electrochemical generators, J. Power Sources 119 (2003) 88−94.

[19] T. Yuan, Z. Tan, C. Ma, J. Yang, Z.-F. Ma, S. Zheng, Challenges of Spinel Li4Ti5O12 for Lithium-Ion Battery Industrial Applications, Adv. Energy Mater. 7 (2017) 1601625−1601650.

[20] J. C. Daigle, Y. Asakawa, M. Beaupré, R. Vieillette, D. Laul, M. Trudeau, K. Zaghib, New Avenue for Limiting Degradation in NanoLi4Ti5O12 for Ultrafast-Charge Lithium-Ion Batteries: Hybrid Polymer−Inorganic Particles, Nano Lett., 17 (2017) 7372−7379.

[21] D. Andre, S-J. Kim, P. Lamp, S. F. Lux, F. Maglia, O. Paschos, B. Stiaszny, Future generations of cathode materials: an automotive industry perspective, J. Mater. Chem. A 3 (2015) 6709-6732.

[22] Y. Maletin, N. Stryzhakova, S. Zelinskyi, S. Chernukhin, D. Tretyakov, H. Mosqueda, N. Davydenko, D. Drobnyi, New Approach to Ultracapacitor Technology: What it Can Offer to Electrified Vehicles, J. Energy Power Eng. 9 (2015) 585-591.

[23] D. Ruan, Y. Huang, L. Li, J. Yuan, Z. Qiao, A Li4Ti5O12+AC/LiMn2O4+AC hybrid battery capacitor with good cycle performance, J. Alloys and Compounds 695 (2017) 1685-1690.

[24] I. Belharouak, G.M. Koenig Jr., T. Tan, H. Yumoto, N. Ota, K. Amine, Performance Degradation and Gassing of Li4Ti5O12/LiMn2O4 Lithium-Ion Cells, J. Electrochem. Soc. 159 (2012) A1165.

[25] K. Wu, J. Yang, Y. Zhang, C. Wang, D. Wang, Investigation on Li4Ti5O12 batteries developed for hybrid electric vehicle, J. Appl. Electrochem. 42 (2012) 989–995.

[26] Z. An, X. Xu, L. Fan, C. Yang, J. Xu, Investigation of Electrochemical Performance and Gas Swelling Behavior on Li4Ti5O12/Activated Carbon Lithium-Ion Capacitor with Acetonitrile-Based and Ester-Based Electrolytes, Electronics 2021, 10, 2623.

[27] A. Devie, M. Dubarry, B. Y. Liaw, Overcharge Study in Li4Ti5O12 Based Lithium-Ion Pouch Cell I. Quantitative Diagnosis of Degradation Modes, J. Electrochem. Soc. 162 (2015) A1033.

[28] A. Devie, M. Dubarry, H. P. Wu, T. H. Wu, B. Y. Liaw, Overcharge Study in Li4Ti5O12 Based Lithium-Ion Pouch Cell II. Experimental Investigation of the Degradation Mechanism, J. Electrochem. Soc. 163 (2016) A2611.

[29] N. Gauthier, C. Courrèges, J. Demeaux, C. Tessier, H. Martinez, Probing the in-depth distribution of organic/inorganic molecular species within the SEI of LTO/NMC and LTO/LMO batteries: A complementary ToF-SIMS and XPS study, App. Surf. Sci. 501 (2020) 144266.

[30] T. Nordh, R. Younesi, M. Hahlin, R. F. Duarte, C. Tengstedt, D. Brandell, K. Edström, Manganese in the SEI Layer of Li4Ti5O12 Studied by Combined NEXAFS and HAXPES Techniques, J. Phys. Chem. C 120 (2016) 3206–3213.

[31] J. Landesfeind, J. Hattendorff, A. Ehrl, W. A. Wall, H. A. Gasteiger, Tortuosity Determination of Battery Electrodes and Separators by Impedance Spectroscopy, J. Electrochem. Soc. 163 (2016) A1373.

[32] T. T. Nguyen, A. Demortière, B. Fleutot, B. Delobel, C. Delacourt, S. J. Cooper, The electrode tortuosity factor: why the conventional tortuosity factor is not well suited for quantifying transport in porous Li-ion battery electrodes and what to use instead. npj Comput. Mater. 6 123 (2020) 123.

[33] G. Martínez-Criado, J. Villanova, R. Tucoulou, D. Salomon, J.-P. Suuronen, S. Labouré, C. Guilloud, V. Valls, R. Barrett, E. Gagliardini, Y. Dabin, R. Baker, S. Bohic, C. Cohen and J. Morse, ID16B: a hard X-ray nanoprobe beamline at the ESRF for nano-analysis, J. Synchrotron Radiat. 23 (2016) 344–35.

[34] P. Cloetens, W. Ludwig, J. Baruchel, Holotomography: Quantitative phase tomography with micrometer resolution using hard synchrotron radiation X rays, Appl. Phys. Lett. 75 (1999) 2912-2914.

[35] C. Hintermüller, F. Marone, A. Isenegger, M. Stampanoni, Image processing pipeline for synchrotron-radiation-based tomographic microscopy, J. Synchrotron Radiat. 17 (2010) 550-559.

[36] J. Schindelin, I. Arganda-Carreras, E. Frise, V. Kaynig, M. Longair, T. Pietzsch, S. Preibisch, C. Rueden, S. Saalfeld, B. Schmid, J.-Y. Tinevez, D. J. White, V. Hartenstein, K. Eliceiri, P. Tomancak, A. Cardona, Fiji: an open-source platform for biological-image analysis, Nat. Methods 9 (2012) 676-682.

[37] Y. K. Chen-Wiegart , R. DeMike, C. Erdonmez, K. Thornton, S. A. Barnett, J. Wang, Tortuosity characterization of 3D microstructure at nano-scale for energy storage and conversion materials, J. Power Sources 249 (2014) 349-356.

[38] G. Ashiotis, A. Deschildre, Z. Nawaz, J. P. Wright, D. Karkoulis, F. E. Picca, J. Kieffer, The fast azimuthal integration Python library: pyFAI, J. Appl. Crystallogr. 48 (2015) 510–519.

[39] B. H. Toby, R. B. Von Dreele, GSAS-II: the genesis of a modern open-source all purpose crystallography software package, J. Appl. Crystallogr. 46 (2013) 544-549.

[40] J. Zheng, J. Xiao, Z. Nie, J. -G. Zhang, Lattice Mn^{3+} behaviors in $Li_4Ti_5O_{12}/LiNi_{0.5}Mn_{1.5}O_4$ full cells, J. Electrochem. Soc. 160 (2013) A1264-A1268.

[41] D. K. Kim, P. Muralidharan, H.-W. Lee, R. Ruffo, Y. Yang, C. K. Chan, H. Peng, R. A. Huggins, Y. Cui, Spinel $LiMn_2O_4$ nanorods as lithium ion battery cathodes, Nano Letters 8 (2008) 3948-3952.

[42] T. Yuan, Z. Tan, C. Ma, J. Yang, Z.-F. Ma, S. Zheng, Challenges of Spinel Li4Ti5O12 for Lithium- Ion Battery Industrial Applications, Adv. Energy Mater. 7 (2017) 1601625.

[43] B.-G. Lee, S.-H. Lee, Application of hybrid supercapacitor using granule Li4Ti5O12/activated carbon with variation of current density, J. Power Sources 343 (2017) 545–549

[39] D. Kim, S. Park, O. B. Chae, J. H. Ryu, Y.-U. Kim, R.-Z. Yin, S. M. Oh, Re-Deposition of Manganese Species on Spinel LiMn2O4 Electrode after Mn Dissolution, J. Electrochem. Soc. 159 (2012) A193.

[44] T. Hildebrand, P. Rüesgsegger, A new method for the model-independent assessment of thickness in three-dimensional images, J. Microsc., 185 (1996) 67-75.

[45] M. Widmaier, N. Jäckel, M. Zeiger, M. Abuzarli, C. Engel, L. Bommer, V. Presser, Influence of carbon distribution on the electrochemical performance and stability of lithium titanate based energy storage devices, Electrochimica Acta 247 (2017) 1006–1018.

[46] A. G. Kashkooli, E. Foreman, S. Farhad, D. U. Lee, W. Ahn, K. Feng, V. De Andrade, Z. Chen, Synchrotron X-ray nano computed tomography based simulation of stress evolution in LiMn2O4 electrodes, Electrochimica Acta 247 (2017) 1103-1116.

[47] Z. Liu, K. Han, Y. K. Chen-Wiegart, J. Wang, H. H. Kung, J. Wang, S. A. Barnett, K. T. Faber, X-ray Nanotomography Analysis of the Microstructural Evolution of LiMn2O4 Electrodes, J. Power Sources, 360 (2017) 460-469.

[48] X. Bai, T. Li, Y.-J. Bai, Capacity degradation of Li4Ti5O12 during long-term cycling in terms of composition and structure, Dalton Trans. 49 (2020) 10003-10010.

[49] H.-C. Chiu, X. Lu, J. Zhou, L. Gu, J. Reid, R. Gauvin, K.Zaghib, G. P. Demopoulos, Capacity Fade Mechanism of Li4Ti5O12 Nanosheet Anode, Adv. Energy Mat. 7 (2017) 1601825.

[50] A. Banerjee, B. Ziv, S. Luski, D. Aurbach, I. C. Halalay, Review—Multifunctional Materials for Enhanced Li-Ion Batteries Durability: A Brief Review of Practical Options, J. Electrochem. Soc. 164 (2017) A6315.

[51] D.R. Vissers, Z. Chen, Y. Shao, M. Engelhard, U. Das, P. Redfern, L.A. Curtiss, B. Pan, J. Liu, K. Amine, Role of manganese deposition on graphite in the capacity fading of lithium ion batteries, ACS Appl. Mater. Interfaces, 8 (2016), 14244-14251.

Figure with captions

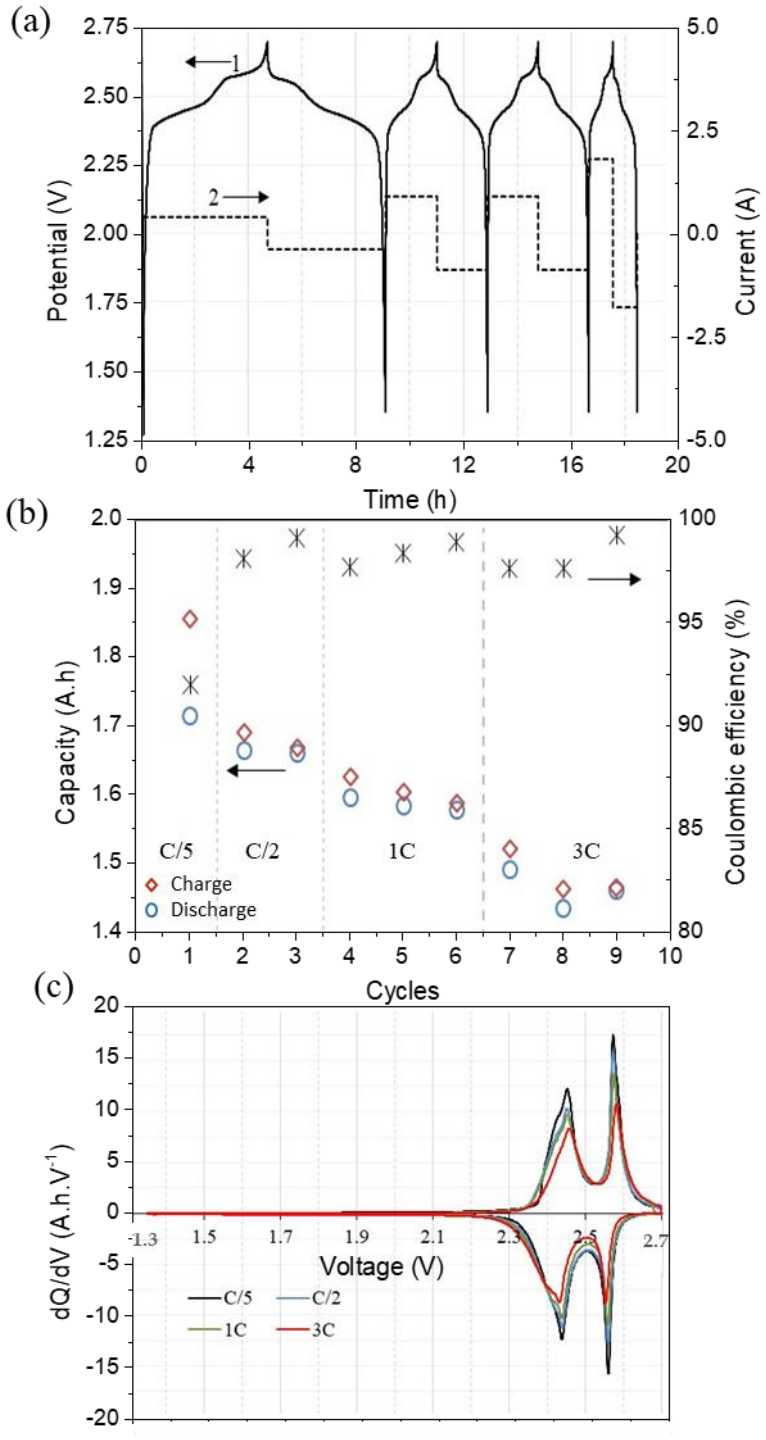

Figure 1 (a) Voltage evolution the pouch cell during the first four cycles of the formation procedure. (b) Capacity (charge/discharge) and coulombic efficiency

of the pouch cell along the entire formation process and (c) corresponding incremental capacity curves for the last cycle of each C-rate change step.

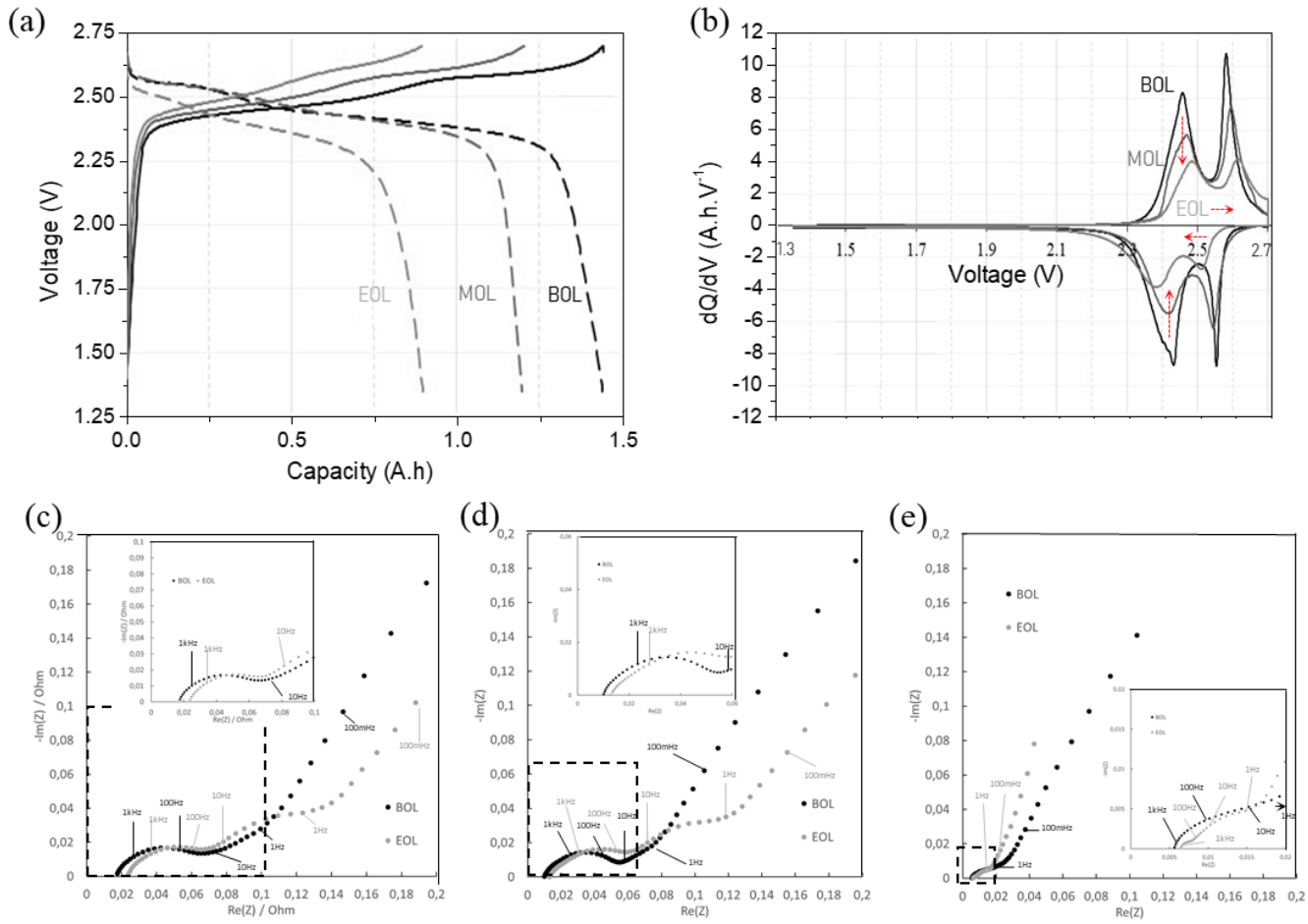

Figure 2 (a) Charge/discharge voltage *vs.* capacity curves at i= 0.5A (C/3) of the pouch cell at the BOL, MOL and EOL states, (b) corresponding incremental capacity curves and EIS spectra for (c) the complete cell, (d) the negative and (e) positive electrode *vs.* LFP reference electrode. U = 5mV at OCP, 8 points per decade between 200 kHz-10mHz.

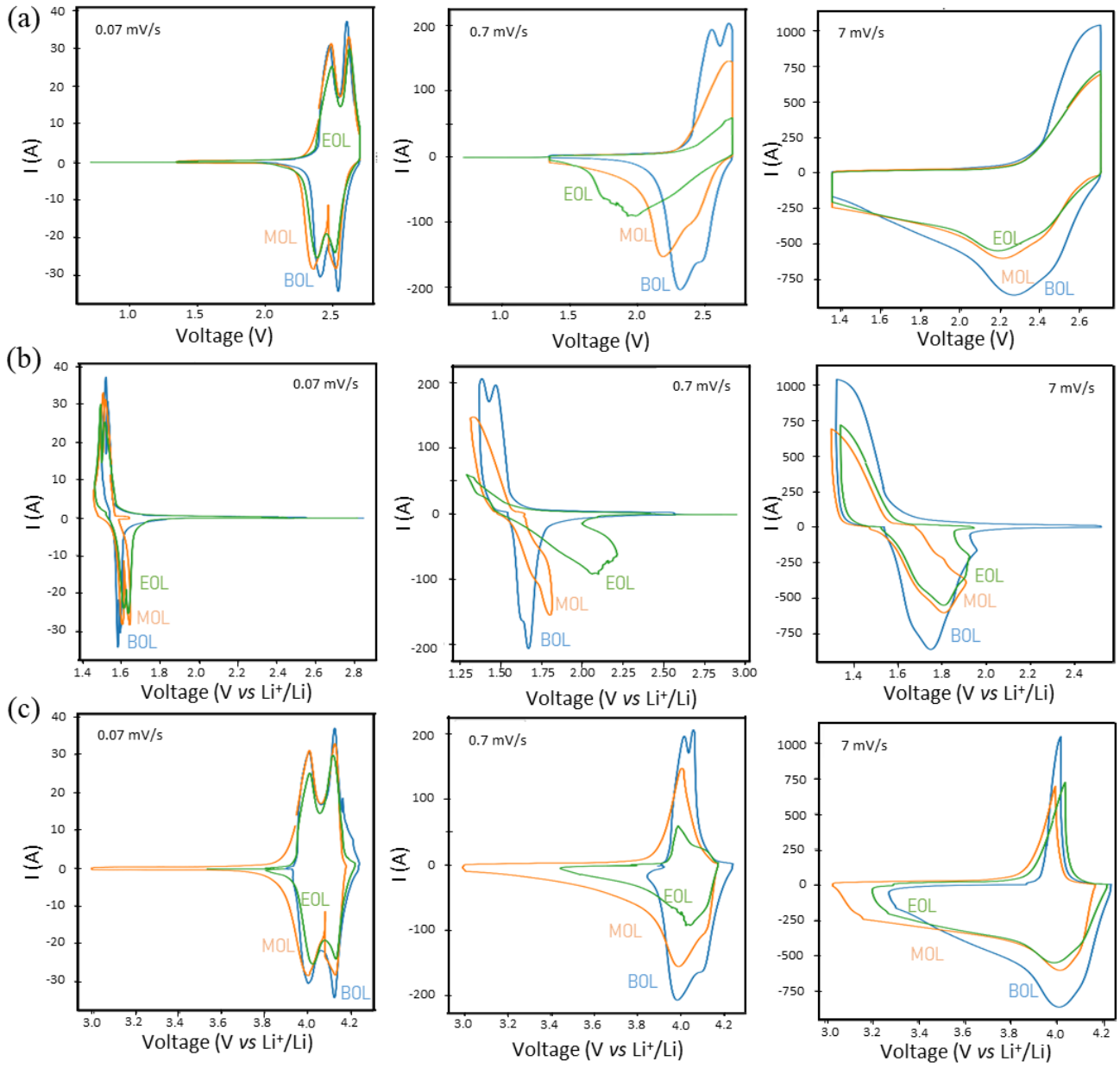

Figure 3 Cyclic voltammetry of the pouch cell at the BOL, MOL and EOL states at different sweep rate (0.07 left to 0.7 middle 7 mV/s right) for (a) the complete cell, (b) the negative and (c) positive electrode vs. LFP reference electrode

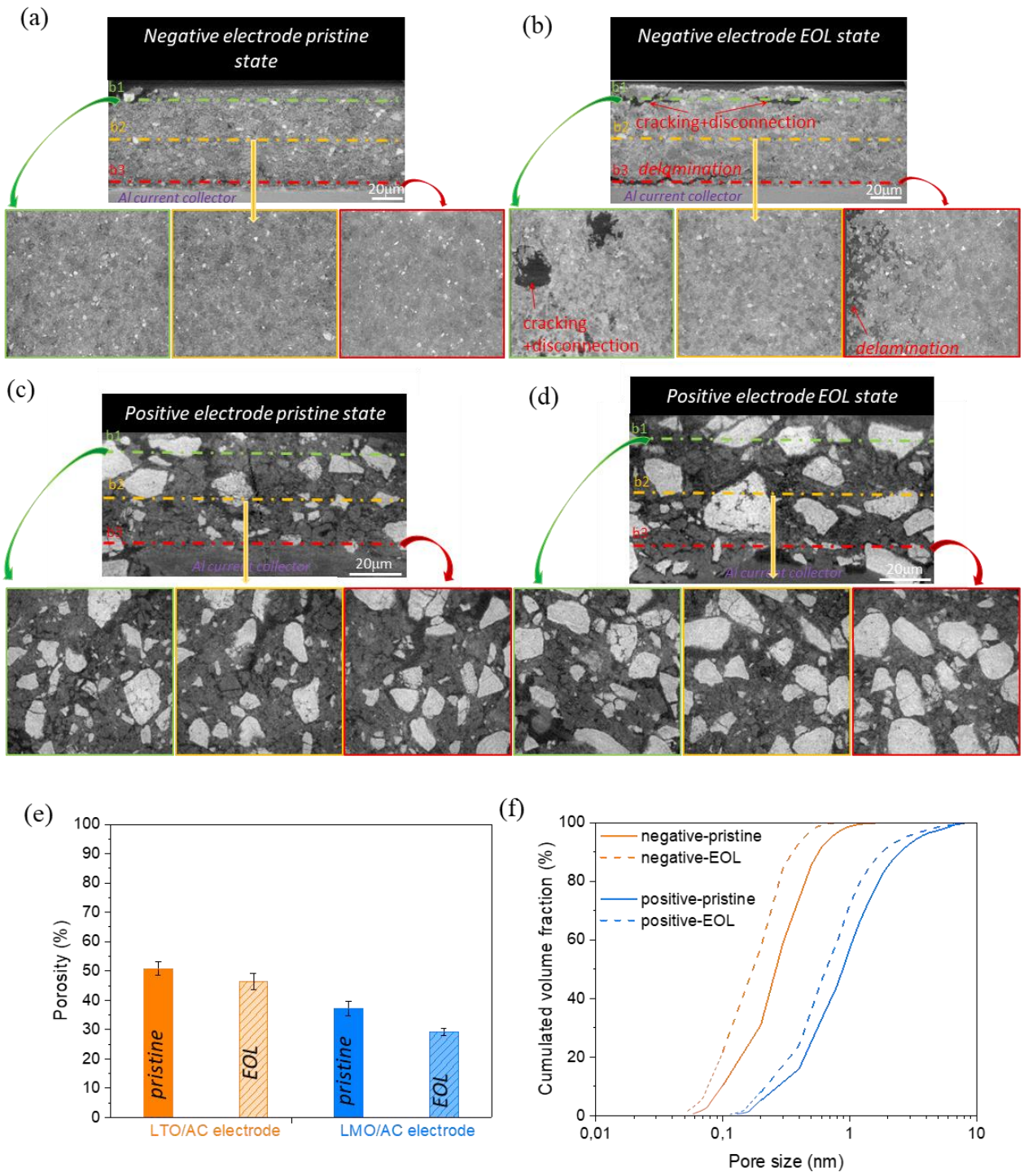

Figure 4 Transversal images of the LTO/AC negative electrode at (a) the pristine and (b) EOL state, with lateral images corresponding to the dashed colored lines on the cross section image; and similarly (c), (d) for the LMO/AC positive electrode. (e) Porosity volume fraction and (f) corresponding pore size distribution at the pristine and EOL state for both negative (orange) and positive electrode (blue).

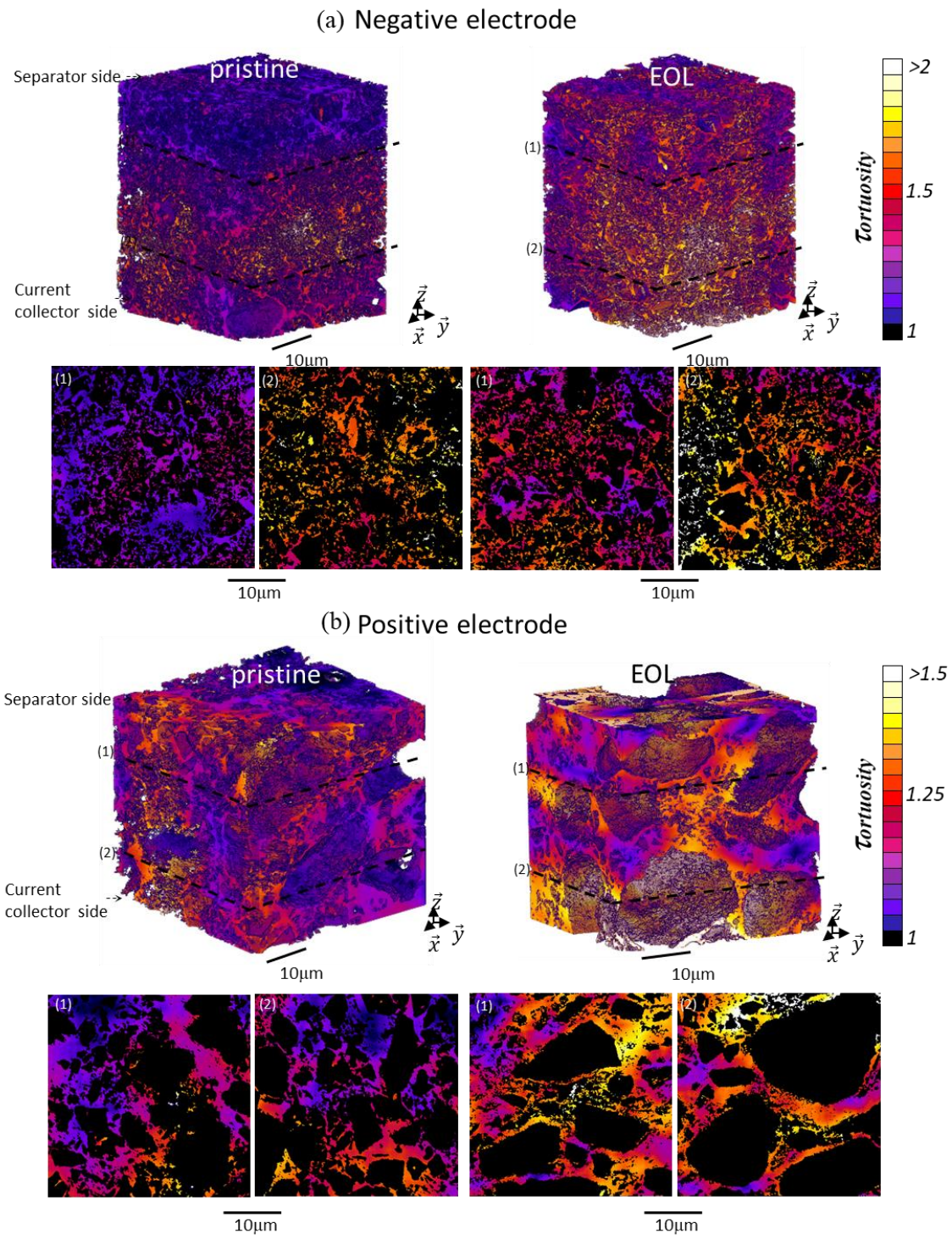

Figure 5 3D color-scale renderings of the effective path distance distribution along the pores network of the (a) LTO/AC electrode at the pristine and EOL state; and (b) LMO/AC electrode. The inserted 2D images below the 3D renderings are transversal slices at different heights across the electrode's thickness and corresponding to the dashed lines represented on the volume images.

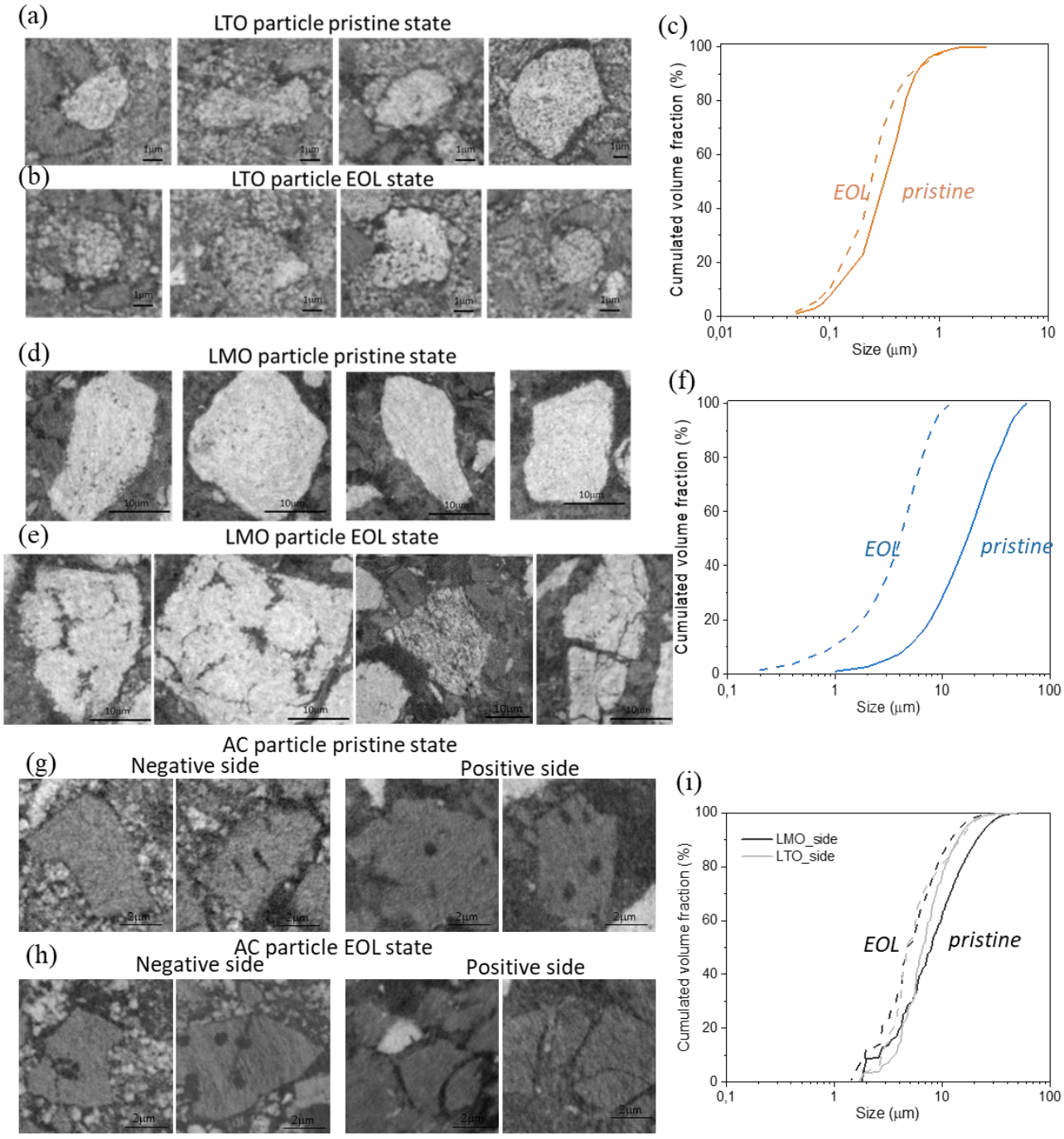

Figure 6 Close-up views of active material particles of (a, b) LTO, (d, e) LMO and (g, h) AC at the pristine and EOL state respectively; and corresponding size distributions for (c) the LTO, (f) LMO and (i) AC at the pristine (plain line) and EOL (dash line) states.

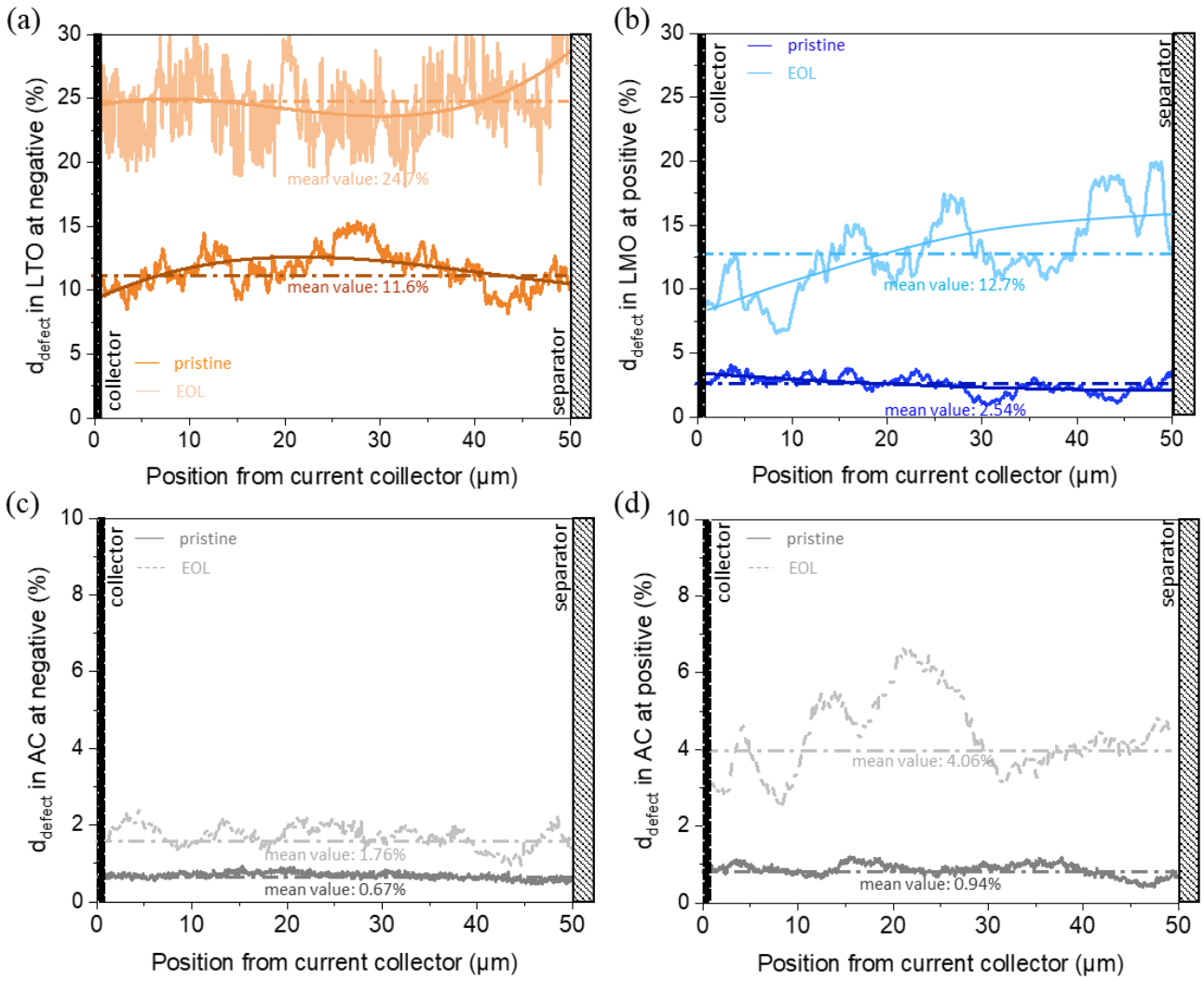

Figure 7 Density of defects detected over the corresponding active material fraction as a function of the distance to the current collector for (a) LTO and (c) AC at the negative electrode; and (b) LMO and (d) AC at the positive electrode.

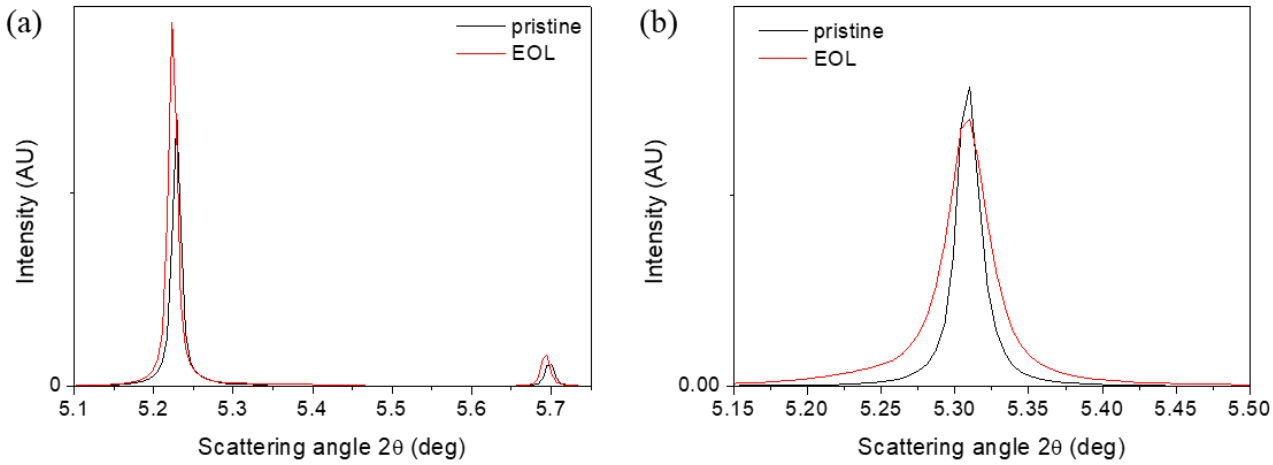

Figure 8 X-ray diffractograms of (a) the LTO 400 and 333 reflections and (b) the LMO 400 reflection at pristine (black line) and EOL (red line).

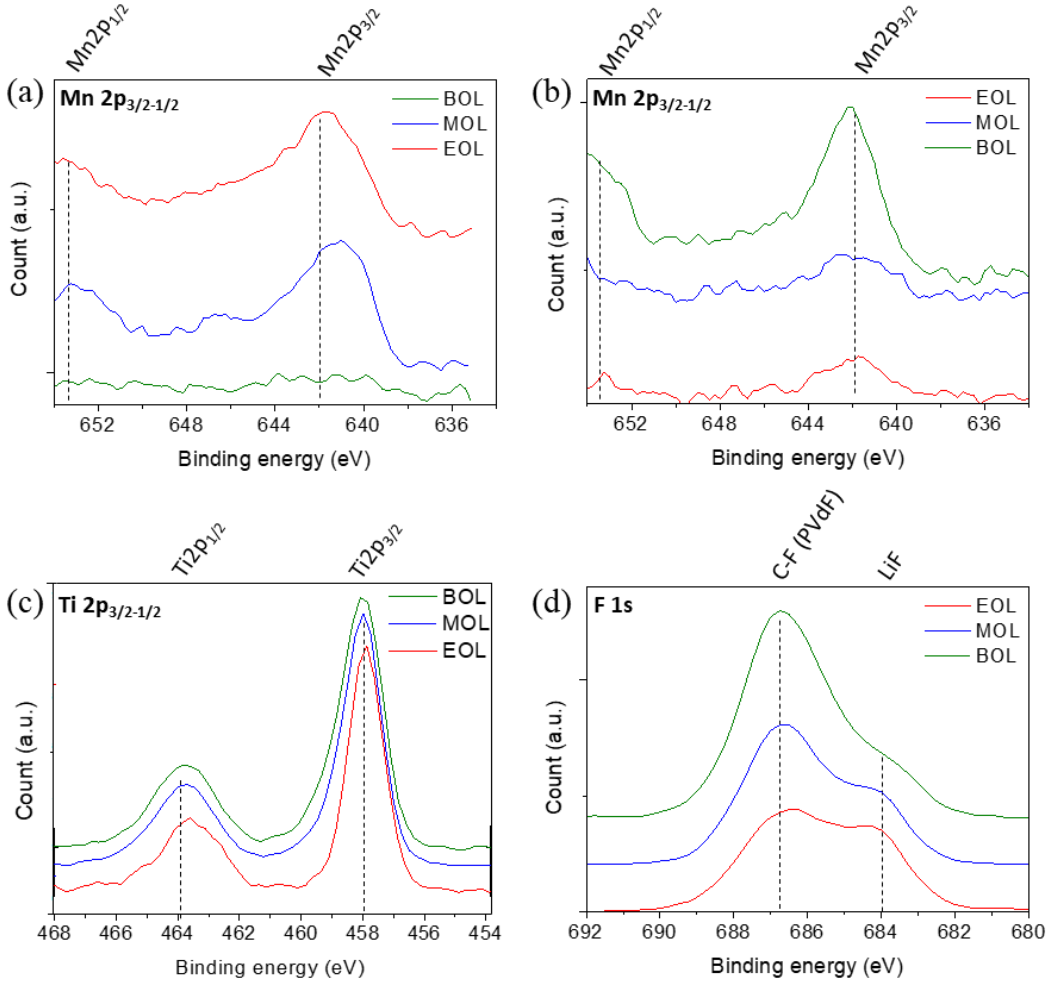

Figure 9 XPS $Mn2p_{3/2}$ core level spectra recorded at the surface of (a) LTO/AC and (b) LMO/AC electrodes at the BOL, MOL and EOL state of cycle life. (c) $Ti2p_{3/2-1/2}$ and (d) F1s core level peak recorded respectively at the surface of LTO/AC and LMO/AC electrodes at different state of cycle life (BOL, MOL, EOL).